Applied Catalysis B: Environmental xxx (xxxx) 121604

Contents lists available at ScienceDirect

Applied Catalysis B: Environmental

journal homepage: www.elsevier.com/locate/apcatb

Nature and role of Cu(II) species in doped C12A7 catalysts for soot oxidation

Isaac Meza-Trujillo [a], Arnaud Mary [a], Piotr Pietrzyk [b], Zbigniew Sojka [b], Eric M. Gaigneaux [a, *]

[a] Institute of Condensed Matter and Nanosciences, UCLouvain, Place Louis Pasteur, 1, Box L4.01.09, 1348 Louvain-la-Neuve, Belgium
[b] Faculty of Chemistry, Jagiellonian University, ul. Gronostajowa 2, 30-387 Krakow, Poland

ARTICLE INFO

Keywords:
Catalytic soot oxidation
Copper
Doped C12A7
Mayenite
Solution combustion synthesis

ABSTRACT

Two series of copper-doped mayenite catalysts ($Cu_x:C_{12-x}A_7$) were synthesized by one-pot-assisted solution combustion at different Cu loadings ($0.06 \leq x \leq 1$) with the aim to correlate their performances in soot combustion and the nature and abundance of the different copper species present. The atmosphere composition influence, precisely of the presence of water, was also studied. It appears that Cu(II) interacted with the C12A7 matrix in three structurally different forms: isolated-Cu^{2+}, clustered-Cu^{2+}, and bulky CuO particles. Cu-C12A7 catalysts exhibited enhanced activity over bare-C12A7, both in terms of soot oxidation at low temperatures and CO_2 selectivity. The control over the dispersion of Cu, the texture, and superoxide concentration of the Cu-C12A7 catalysts achieved by adjusting the Cu loading and calcination temperature, appeared crucial in promoting the catalytic performance. We concluded that the well-dispersed clustered Cu^{2+} is the most likely active species responsible for the improved activity both under dry and wet conditions.

1. Introduction

Nowadays, despite the growing market interest in betting for non-conventionally greener vehicle engines, like hybrid and electric powered ones, still, more than 95% of the commercially available vehicles are based on conventional fuels [1], whose exhaust emissions are undoubtedly linked to several health hazards and environmental issues [2,3]. Historically, diesel engines have been considered the principal source of particulate matter (PM), colloquially referred to as "soot". However, since the introduction of the gasoline direct injection (GDI) engine as a more efficient system over the traditional port fuel injection (PFI) one, the PM mass emissions turned out to be a critical issue for gasoline engines as well [4]. In the last decades, enforced emission regulations (i.e., Euro VI) have been implemented to control PM limit discharges (0.005 g km^{-1}) [3]. Since the onset temperature for the spontaneous combustion of soot (>600 °C) is higher than those of the exhaust gas (200–500 °C) [5], exhaust after-treatment technologies (i.e., catalytic diesel/gasoline particulate filters) have been proposed as alternatives to accelerate the soot oxidation rate at low temperatures.

Catalytic soot oxidation is an intricate process with three counterparts (soot particles, catalyst, and exhaust gases), which takes place at the interface contact points between the two solids and the gas stream. The direct soot oxidation via the active oxygen mechanism involves the activation of dioxygen molecules on the catalyst surface and subsequent transfer (via spillover) of the highly reactive oxygen species (peroxide and superoxide radicals) to soot particles [6,7]. Nowadays, the most active catalysts in soot combustion are based on noble metals (e.g., platinum group) [8,9], rare metal oxides (e.g., pure or doped CeO_2) [6,10,11], or a combination of both [12–15]. However, these materials are scarce and expensive, which limits their mass manufacture. On top of this, and despite their high efficiency, these catalysts suffer from several drawbacks such as poisoning [16], sintering [12,17], and thermal instability [5,6] due to the exothermicity of the oxidation reaction between soot and oxygen, which could raise the temperature inside the filter to ca. 1000 °C or even higher at localized hot spots [5,14]. Therefore, the development of competitive soot oxidation catalysts using neither noble nor rare metals is of great interest for commercial and environmental reasons.

In this aim, numerous researches have explored alternative materials to catalyze soot oxidation, such as perovskites [18], MnO_x [19,20], spinels [21], and other metal oxides [22,23]. Among the latter, a calcium aluminate called mayenite ($12CaO{\cdot}7Al_2O_3$ hereafter C12A7) that consists of highly abundant and inexpensive elements has been shown to accelerate the total decomposition of soot at lower temperatures than that required for spontaneous combustion [22]. C12A7 possesses a peculiar structure featured by 12 nanocages per unit cell with an inner space of ~0.4 nm, embedded in a positively charged framework, $[Ca_{24}Al_{28}O_{64}]^{4+}$, and capable of hosting several reactive oxygen species (O_2^-, O_2^{2-}, and O^-) as counter-anions. These species have been recognized as the accountable ones for its catalytic activity [22,24]. We pre-

* Corresponding author.
E-mail address: eric.gaigneaux@uclouvain.be (E.M. Gaigneaux).

https://doi.org/10.1016/j.apcatb.2022.121604
Received 3 March 2022; Received in revised form 31 May 2022; Accepted 4 June 2022
0926-3373/© 20XX

viously showed that the enhancement of C12A7′s textural properties (i.e., specific surface area) improved its catalytic performances in soot oxidation, demonstrating to be more active and selective towards CO_2 than the non-porous one [23]. Similarly, other studies have reported that the inclusion of foreign cations within the framework of C12A7 as dopants can lead to a substantial amelioration of the electronic and catalytic properties of mayenite [25]. The lower price of transition metals in comparison to noble metals makes them promising contenders for practical application in soot elimination. Among different dopants (Co, Fe, Cr, Cu and Ni), a Si-containing C12A7 ($Ca_{12}Al_{10}Si_4O_{35}$) co-doped with Cu and synthesized via hydrothermal reaction has shown the best catalytic activity in the soot oxidation. Sato et al. suggested that the partial replacement of Ca^{2+} ions by foreign metal ions leads to a reactivity enhancement of the occluded O_2^- species [22]. Yet the nature of the copper species interacting with the reactive oxygen species remained uncertain in the latter study. Besides, Maurelli et al. studied the localization of Cu^{2+} ions and their interactions with native anions (O_2^- and OH^-) in a Cu-doped C12A7 using EPR spectroscopy [26]. Cu-substituted C12A7 was synthesized by impregnating an already-prepared undoped C12A7 (obtained via solid-state reaction) with an ethanolic solution containing Cu nitrate and calcining at 900 °C for 0.5 h. They revealed the existence of three different Cu^{2+} species inside the C12A7 framework, presenting axial symmetry and well-resolved parallel hyperfine structure, which is characteristic of isolated divalent copper species ($Cu^{2+}(d^9)$, $S = ½$, $I = 3/2$). They established that Cu^{2+} centers interacted directly with OH^- occluded ions located in the same or nearby cages, while O_2^- extra-framework species preferentially interacted with Ca^{2+} ions. Recently, a theoretical study suggested that the partial incorporation of copper in C12A7 electride form (C12A7:e-) can facilitate the formation of a conduction channel, which could boost the electronic conductivity of this material [27]. To the best of our knowledge, none of these previous reports have described the role of copper species in the catalytic activity enhancement of Cu-doped C12A7 in soot combustion. Nor has reported on the nature of other kinds of copper species that could be formed during the synthesis of Cu-C12A7 materials, whose presence could also influence the catalytic performances of these catalysts.

In the present contribution, we therefore have investigated the outcomes of preparing Cu-C12A7 catalysts with ranging copper contents, presenting different textural properties and superoxide concentrations by controlling the calcination temperature via a one-pot-assisted solution combustion synthesis approach. Herein, we have attempted to assess which copper species (isolated Cu^{2+}, well-dispersed Cu^{2+} clusters, or segregated bulk CuO particles) are responsible for the enhancement of the catalytic soot conversion and CO_2 selectivity via a detailed analysis of the physicochemical properties of the Cu-C12A7 catalysts using different analytical techniques, namely PXRD, N_2 physisorption, XPS, EPR, and Raman spectroscopies. Finally, to determine the influence that the atmosphere composition of the engine exhaust gases could have over the catalytic activity of our Cu-C12A7 catalysts, the soot oxidation was also performed in the presence of water vapor (5% H_2O + 5% O_2/He, wet conditions) to corroborate our findings obtained under dry conditions (5% O_2/He).

2. Materials and methods

2.1. Materials

Materials employed during the synthesis of Cu-doped C12A7 such as aluminum nitrate nonahydrate ($Al(NO_3)_3{\cdot}9H_2O$, ≥ 99%), calcium nitrate tetrahydrate ($Ca(NO_3)_2{\cdot}4H_2O$, ≥ 99%), copper(II) nitrate hemi (pentahydrate) ($Cu(NO_3)_2{\cdot}2.5H_2O$, ≥ 99%), urea (CH_4N_2O, ≥99%), β-alanine ($C_3H_7NO_2$, ≥99%), and anhydrous oxalic acid ($C_2H_2O_4$, ≥99%) were purchased from Merck. All products were used as delivered without any further treatments.

2.2. Cu-doped C12A7 preparation

The protocol to prepare Cu-doped C12A7 catalyst via one-pot assisted solution combustion synthesis is schematized in Fig. 1. The catalysts are denoted as Cu(*x*)-C12A7-*Y*, where "*x*" stands for the nominal molar fraction of Ca replaced by Cu, and "*Y*" represents the calcination temperature. Regarding the preparation of non-doped C12A7 porous material, a detailed description can be found elsewhere [23].

All reagent amounts, except oxalic acid, were calculated based on the overall combustion reaction Eq. (1), with an oxidizer/fuel ratio equal to 1 (φ = 1, stoichiometric conditions). The overall combustion is described as follows:

$$\begin{aligned} & x\ Cu\ (NO_3)_2 + (12 \\ & -\ x)\ Ca(NO_3)_2 + 14\ Al(NO_3)_3 \\ & +\ 55/2\ \phi\ CH_4N_2O \\ & +\ 11\ \phi\ C_3H_7NO_2 \\ & +\ 165/2\,(\phi\ -\ 1)\ O_2 \rightarrow Cu_xCa_{(12-x)}Al_{14}O_{33} \\ & +\ 121/2\ \phi\ CO_2 + 187/2\phi\ H_2O \\ & +\ 33\ (\phi + 1)\ N_2 \end{aligned} \quad (1)$$

Stoichiometric quantities of metal nitrates (Cu/Ca/Al:*x*/12-*x*/14) and fuels (urea/β-alanine:27.5/11) to produce 5 g of Cu-doped C12A7 per batch were added into an open borosilicate glassware container (300 mL) and dissolved with ca. 5 mL of preheated distilled water (80 °C) under magnetic stirring at 80 °C. Next, a specific amount of oxalic acid (OA) (0.5 g per g of C12A7 to be produced) was dissolved in ~3 mL of preheated distilled water (80 °C) and added to the former solution. Once a whitish light blue solution was obtained, the open pot, containing the homogenous solution, was placed in a preheated furnace at 500 °C to trigger the combustion reaction. As soon as the ignition temperature was attained, an exothermic self-sustaining reaction took place with the occurrence of glowing reddish flames (Fig. A.1, see Appendix A), giving way to a solid product in a matter of a few seconds (~15 s). The as-synthesized solid product was manually ground and mixed with distilled water (80 °C) to form a slurry with a mass ratio of 1 g/100 g (solid/water) and stirred for about 20 min. Then, the slurry was filtered and the retained wet-solid was dried overnight at 120 °C. Finally, the as-dried powder was hand-ground and calcined between 600 and 800 °C in a preheated furnace for 4 h under static air, then it

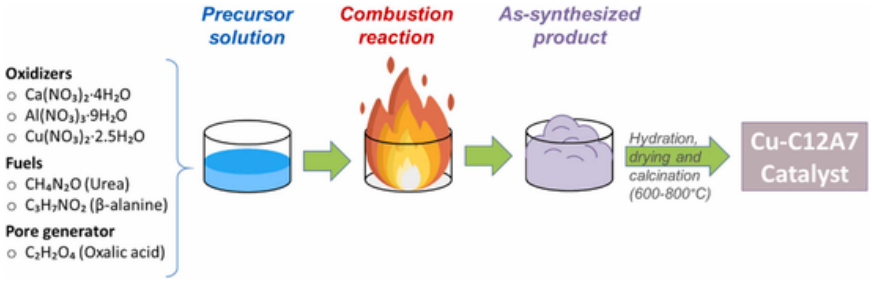

Fig. 1. Scheme for Cu(*x*)-C12A7 catalyst preparation via one-pot solution combustion assisted synthesis.

was cooled down to room temperature and stored for further characterizations.

2.3. Characterizations

Powder X-ray diffraction (PXRD) patterns were recorded on a Bruker-D8 advance diffractometer (Bragg-Brentano geometry), equipped with a LYNXEYE XE-T detector, using Cu Kα radiation (λ = 0.15418 nm). The X-ray source was operated with a voltage of 40 kV and a current of 30 mA. Diffractograms were collected between 10° and 80° (2θ) with a scan size of 0.02°(2θ) and scanning rate of 3.8°·min^{-1} . The data visualization and phases identification were accomplished using the software DIFFRAC.SUITE EVA and the PDF2–2004 database. The crystallite size was calculated from the (*2 1 1*) reflection, using Scherrer's equation.

Textural properties were evaluated via nitrogen physisorption at − 196 °C in the relative pressure (P/Po) region of 0.01–0.99, using a Micromeritics Tristar 3000. Prior to the analysis, the sample (~0.15 g) was degassed overnight under vacuum (ca. 1.3 × 10^{-4} bar) at 300 °C. The specific surface area was evaluated with the BET method in the range of 0.05–0.3 (P/Po). The pore size distribution was obtained via BJH method from the desorption isotherm branch.

Electron paramagnetic resonance (EPR) spectra were recorded at ~9.4 GHz microwave frequency (X-band) and 100 kHz modulation frequency at liquid nitrogen temperature (77 K) using a Bruker ELEXSYS 500 spectrometer. A microwave power of 2 mW and a modulation amplitude between 0.2 and 0.5 mT was applied. The spectra processing was carried out using the software provided by Bruker, while the spin concentrations of paramagnetic species were determined from the second integral of the spectra using $CuSO_4$ as a standard. For each spectrum, the contributions of the various paramagnetic superoxide and copper(II) species were determined by computer simulation using the program EPRsim32 [28]. The cumulative error from quantification by comparison with the standard and the simulation is estimated at ca. 20%.

X-ray photoelectron spectroscopy (XPS) analyses were carried out using an SSX 100/206 spectrometer (Surface Science Instruments, USA) with Al-Kα radiation operated at 10 kV and 20 mA. Powdered samples were pressed into stainless-steel troughs of 6-mm diameter positioned on a ceramic carrousel. The pressure in the analysis chamber was ~10^{-6} Pa. The analyzed area was ~1.4 mm^2 and the pass energy was set at 150 eV. A flood gun set at 8 eV and a Ni grid placed 3 mm above the sample surface were used for charge compensation. The following sequence of spectra was recorded: survey spectrum, C 1s, O 1s, Al 2p Ca 2p, Cu 2p and C 1s again to check the stability of charge compensation with time. The binding energy scale was referenced to the C-(C,H) component of the C 1s peak of adventitious carbon contamination fixed at 284.8 eV. Data treatment was performed with the CasaXPS program (Casa Software Ltd, UK). The spectra were decomposed with the least-squares fitting routine provided by the software with a Gaussian/Lorentzian (85/15) product function after subtraction of a non-linear Shirley baseline. Atomic concentrations were calculated using peak areas normalized based on the acquisition parameters and sensitivity factors provided by the manufacturer.

The Raman spectra were collected on an InVia Renishaw spectrometer coupled with a confocal microscope (Leica DM LM) using an x50 objective lens, equipped with an 1800 l/mm grating, a slit opening of 65 μm, and a CCD detector. The spectra were recorded between 100 and 1600 cm^{-1} , operating at an excitation wavelength of 514 nm (green light) and power of ca. 50 mW. Each spectrum is an average of 8 accumulations.

2.4. Catalytic performance evaluation

The catalytic performance during the soot oxidation over different Cu-C12A7 samples was investigated via temperature-programmed combustion (TPC) employing a frequently used carbon black (CB) powder (Printex U, Degussa) as a diesel soot model [29]. In each catalytic test, 200 mg of soot and catalyst (5%wt of CB) were hand-mixed in a mortar for ~10 min (tight contact conditions). Then, 50 mg of resulting mixture were loaded inside a quartz tube (microreactor, i.d. = 0.4 mm) between two layers of silica wool. All the runs were performed under atmospheric pressure from 50 to 800°C at a heating rate of 10 °C min^{-1} in a CATLAB-PCS Microreactor (Hiden Analytical) coupled to a QGA (Hiden Analytical) mass spectrometer. For dry conditions, an inlet gas flow of 5% O_2 in He (Praxair) was fed at a flow rate of 50 mL min^{-1} . For the experiments performed in the presence of water (wet conditions), the same inlet flow of dry gases went through a saturator (continuous bubbling system) kept inside a thermostatic bath at 33 °C (p_{vH_2O} = 0.05 atm) to humidify the gas stream. All tubing lines downstream the saturator were heated at 50 °C to prevent the vapor condensation. Temperatures corresponding to 10%, 50%, and 90% soot conversion (denoted as T_{10}, T_{50}, and T_{90}, respectively), as well as the temperature (T_{peak}) at which the highest combustion rate is attained (i.e., maximum production of CO_x), determined from the TPC curves, were used as indicators of the activity of the tested catalysts. The produced amounts of CO_2 and CO were obtained by integrating the area under the corresponding curves obtained from the TPC runs. The selectivity towards CO_2 formation to the total amount of CO_x generated during the soot oxidation was calculated via Eq. (2):

$$S_{CO_2}(\%) = 100 \quad \times \quad C_{CO_2} / \left(C_{CO_2} + C_{CO} \right) \tag{2}$$

where C_{CO_2} and C_{CO} are respectively the total concentration of CO_2 and CO obtained by integrating the area underneath the corresponding TPC curve.

3. Results and discussion

3.1. Catalytic combustion of soot

The catalytic performances of two sets of Cu(*x*)-C12A7 catalysts, calcined at 600 and 800 °C were evaluated in the soot oxidation reaction. In the present study, the nominal doping degree (*x*) represents the ratio between the molar fraction of Ca replaced by Cu and the total number of moles of Ca in C12A7, which was ranged between 0.06 and 1. Pristine C12A7 samples (*x* = 0) annealed at the same conditions were also tested for comparison. In this study, all catalysts were evaluated by the thermo-programmed combustion (TPC) method under tight-contact conditions because it ensures in our opinion a better reproducibility than loose contact conditions when preparing the solid mixture (catalyst with soot), even though it is a less representative approximation of the contact between soot particles and catalyst in realistic conditions. Besides, tight contact allows a better understanding of the intrinsic reactivity, which are imperative to draw reliable comparisons between the different catalysts, as reported in the literature [5,6]. The catalytic results, along with an uncatalyzed soot combustion experiment (Printex-U), are shown in Figs. 2 and 3, A.2, and Table 1. The conversion profiles (Fig. 2) were obtained by integrating the area under the TPC CO_x curves (Fig. A.2 see Appendix A) in the temperature range between ~350–580 °C, which is undoubtedly associated with the CO_x produced by the catalytic combustion of soot over Cu-C12A7 catalysts. As previously reported, the minor peaks emerging above ca. 580 °C in the TPC curves are linked to CO_2 released due to the decarbonation of calcium carbonates upon heating over 600 °C approximately [23].

In the absence of catalyst, the highest combustion rate for Printex-U was attained at 606 °C (T_{peak}), while the T_{10}, T_{50}, and T_{90} were 537, 599,

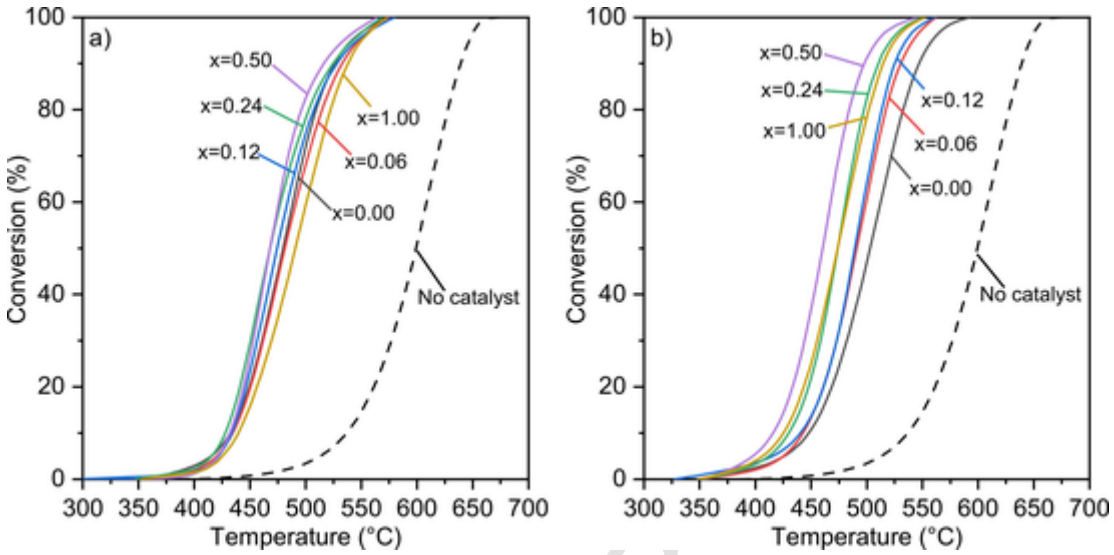

Fig. 2. Profiles of soot conversion over Cu-C12A7 catalysts calcined at (a) 600 and (b) 800 °C.

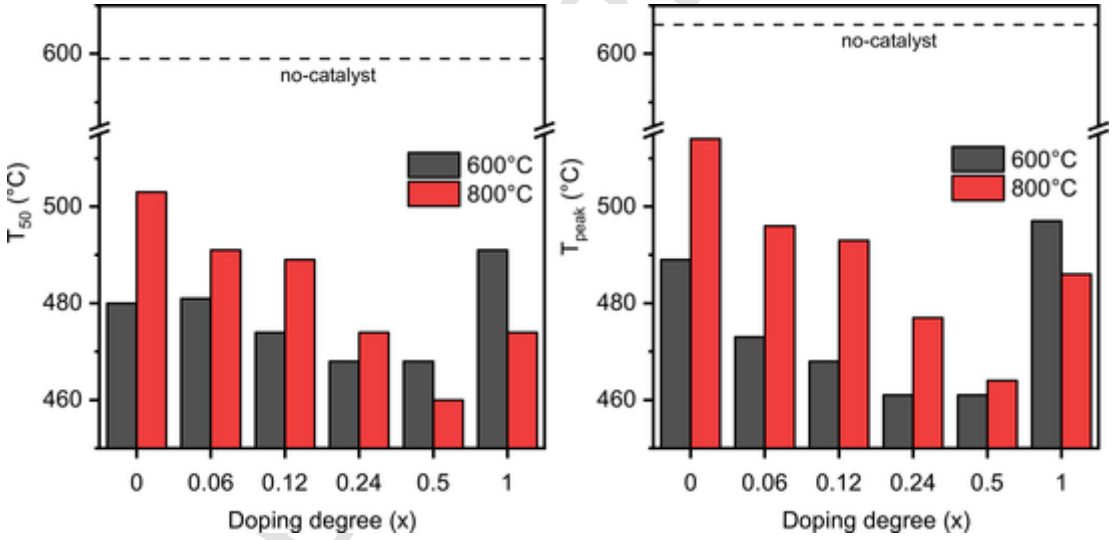

Fig. 3. Comparison of the activity indicators T_{50} and T_{peak} between the two sets of Cu(x)-C12A7 catalysts.

and 639 °C, respectively (entry 13, Table 1). In comparison, after performing the soot combustion in the presence of the catalyst, the soot conversion curve shifts to lower temperatures (Fig. 2), implying that all tested catalysts promote soot combustion. The latter is confirmed by examining the T_{50} (Fig. 3a) and T_{peak} (Fig. 3b) values, demonstrating that all Cu-containing C12A7 samples exhibit T_{50} and T_{peak} values at least 100 degrees below those revealed by the uncatalyzed soot oxidation. Likewise, Cu-doped C12A7 catalysts display enhanced catalytic activities compared to the undoped C12A7 ones, showing the T_{peak} values shifts of 28 and 50 °C for those annealed at 600 and 800 °C, respectively. This positive effect on the catalytic activity (i.e., T_{50} or T_{peak} reduction) increases with rising the copper loading until the highest activity is observed at $x = 0.5$. Further increments in the copper content ($x = 1.0$) lead to activity loss, accomplishing the oxidation of soot at higher temperatures (entries 6 and 12, Table 1).

Similarly, the calcination temperature also has a distinct impact on the catalytic activity. For instance, better results, in terms of T_{10} (onset temperature), are shown by the set of Cu-doped catalysts calcined at 600 °C, than those treated at 800 °C. However, a noticeable reduction in the onset temperature is observed within the catalysts set calcined at 800 °C as copper loading is raised, displaying the lowest T_{10} (416 °C) for a doping degree of $x = 0.5$, among the two series of catalysts. Meanwhile, the onset temperatures remain almost unchanged for all catalysts of the Cu(x)-C12A7–600 series, regardless of the copper content. Regarding the T_{peak}, as the copper content approaches $x = 0.5$, the materials calcined at 600 °C seem to attain a plateau, displaying the same catalytic performance ($T_{peak} = 461$ °C) in the range 0.24–0.5. In the case of the Cu(x)-C12A7–800 series, a nadir is attained at $x = 0.5$ ($T_{peak} = 464$ °C), showing a similar catalytic behavior as the one annealed at 600 °C and bearing the same copper loading. On the other hand, from $x \geq 0.5$, the differences of T_{50} observed between the two Cu-C12A7 series calcined at 600 and 800 °C reveal an inverted behavior, with those annealed at high temperatures exhibiting higher activity. As exposed before, at the highest copper content ($x = 1.0$), the catalytic activity lessens. However, the Cu-containing C12A7 catalyst calcined at 600 °C shows to be even less active than the pristine one ($x = 0$) heat-treated at the same temperature. Conversely, the one annealed at 800 °C, despite its lower activity, still performs better than bare C12A7.

Finally, both series of Cu-doped C12A7 catalysts show a dominant production of CO_2 over CO with regards to the uncatalyzed combustion reaction where CO (66%) is predominantly formed (entry 13, Table 1). Increasing the copper content further promotes the CO_2 selectivity reaching 100% as the doping degree approaches $x = 0.24$ and remains at maximum from thereon. Furthermore, it can be noticed that the se-

Table 1
Catalytic activity indicators and CO_2 selectivity of Cu(*x*)-C12A7 catalysts.

Entry	Catalyst	Doping degree (x)	T_{10} (°C)	T_{50} (°C)	T_{90} (°C)	T_{peak} (°C)	S_{CO_2} (%)
1	C12A7–600	0.0	432	480	527	489	92
2	Cu(0.06)-C12A7–600	0.06	435	481	533	473	92
3	Cu(0.12)-C12A7–600	0.12	433	474	528	468	96
4	Cu(0.24)-C12A7–600	0.24	427	468	525	461	100
5	Cu(0.50)-C12A7–600	0.50	431	468	516	461	100
6	Cu(1.00)-C12A7–600	1.00	440	491	538	496	100
7	C12A7–800	0.0	448	503	547	514	91
8	Cu(0.06)-C12A7–800	0.06	443	491	531	496	92
9	Cu(0.12)-C12A7–800	0.12	440	489	525	493	95
10	Cu(0.24)-C12A7–800	0.24	425	474	510	477	100
11	Cu(0.50)-C12A7–800	0.50	416	460	498	464	100
12	Cu(1.00)-C12A7–800	1.00	425	474	515	486	100
13	Printex U (no catalyst)		537	599	639	606	34

lectivity is independent of the heat treatment history of the sample, showing equivalent CO_2 selectivities among each pair of catalysts for a given copper doping degree, whatever the calcination temperature. This enhancement in the CO_2 selectivity might be associated with the enhanced redox properties of Cu(*x*)-C12A7 catalysts compared to bare-C12A7 due to the introduction of copper, which is known for accelerating the oxidation of CO to CO_2 [21].

From the above considerations, we may determine that the optimum copper content for the oxidation of soot with Cu(*x*)-C12A7 catalysts is close to $x = 0.5$. Therefore, in order to understand the relationship between the catalytic behavior of the studied Cu(*x*)-C12A7 materials and the copper-mayenite interactions, a detailed analysis of their respective physicochemical properties was performed and discussed in the following.

3.2. Catalyst characterization

3.2.1. Structural analysis by powder X-ray diffraction (PXRD) and Raman spectroscopy

The effect of the copper loading and calcination temperature on the crystalline structure of Cu(*x*)-C12A7 catalysts was investigated by PXRD. Fig. 4a and b show the diffractograms of the two series of Cu-doped C12A7 samples calcined under static air conditions at 600 and 800 °C, respectively. Additionally, Table 2 gathers several structural parameters evaluated from the PXRD patterns. The diffractograms of both Cu-doped C12A7 sets (600 and 800 °C) exhibited typical reflections of mayenite-crystal cubic centered structure (*I-43d*), which were identified with the JCPDS No. 09-0413 database reference for this material [30]. The principal peaks at $2\theta = 18.1, 29.7, 33.4, 36.7, 41.2$ and $46.6°$ correspond to the (*2 1 1*), (*4 0 0*), (*4 2 0*), (*5 2 1*) and (*6 1 1*) planes, respectively, which along with other low-intensity labeled peaks (*) are attributed to C12A7 crystal structure. Besides, minor XRD peaks (•) were also identified and ascribed to the CaO crystal phase (JCPDS No. 37-1497). We have previously reported on the production of pristine porous C12A7 via the transformation of a hydrogarnet ($Ca_3Al_2(OH)_{12}$/C3AH6) precursor, which also led to the segregation of the CaO impurity [23]. Here the formation of the C3AH6 phase after hydration and drying of the copper-containing combustion product (*see scheme* Fig. 1)

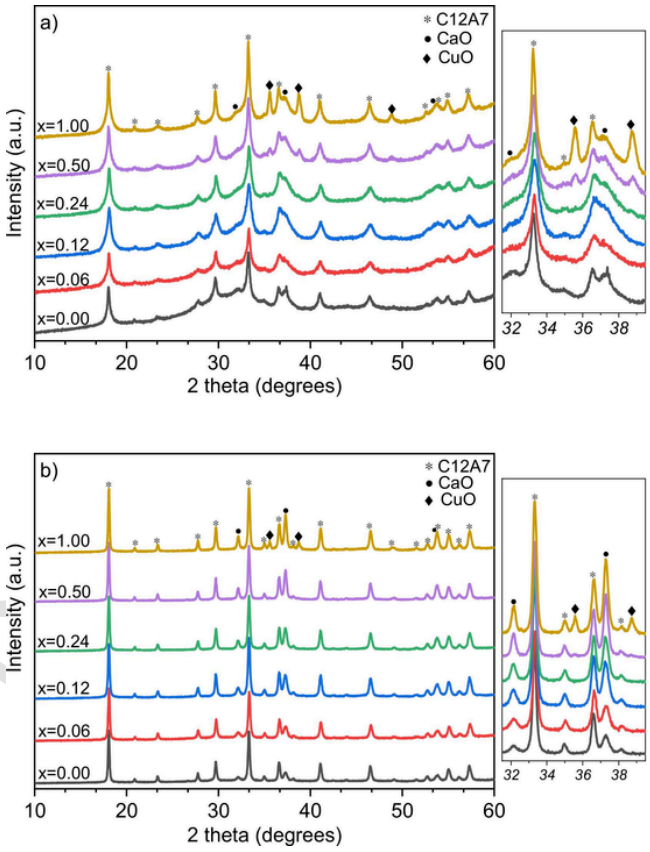

Fig. 4. PXRD patterns of Cu(*x*)-C12A7 samples calcined at (a) 600 and (b) 800 °C for 4 h in static air. For comparison, diffractograms of pristine C12A7 ($x = 0$) are shown at the bottom line of each graph. Insets are shown to guide the reader through the identification of the different phases.

is confirmed by PXRD, as shown in Fig. A.3 (see Appendix A) corroborating our assessments.

Moreover, the characteristic peaks of CuO likely to appear at 35.5 and 38.7° were not distinguished in samples presenting low doping degrees ($x \leq 0.24$). However, at high Cu loadings ($x \geq 0.5$), the formation of a segregated CuO phase (♦) was pointed out, which is more distinguishable on the series calcined at 600 °C due to the lower intensity of C12A7 reflections, as compared to the catalysts calcined at higher temperatures (800 °C) (*see insets* Fig. 4a and b). Hence, the absence of copper-related reflections in the PXRD patterns at low doping degrees suggests that copper is either well-incorporated in the C12A7 matrix forming a solid solution or is well-dispersed on C12A7′s surface. Conversely, at high contents, the presence of CuO reflections indicates the segregation of at least a fraction of the initially introduced copper during the synthesis as a concomitant oxidic phase.

Although, both series of Cu-doped samples exhibit very similar diffractograms among each set of samples, the calcination temperature influences the structural properties of the Cu(*x*)-C12A7 catalysts. At low temperature (600 °C), the slight presence of an amorphous domain is illustrated by a small broad signal in the background line between 25° and 35° (2θ), which tends to disappear with increasing copper loading. Besides, in the enlarged 2θ regions of the set calcined at 800 °C (inset Fig. 4b), the intensity of CaO peaks at $2\theta = 32.2$ (*1 1 1*) and 37.3° (*2 0 0*) continuously increases with rising of the Cu nominal content as compared to the pristine C12A7. These two observations are probably correlated with the modification of the reaction stoichiometry via the partial replacement of Ca by Cu to induce vacancies in the mayenite framework to promote Cu^{2+} insertion. It seems that this alteration in the stoichiometry endorsed the formation of CaO as the doping degree increases for the series calcined at high temperature, whereas at low tem-

Table 2
Characterization results of Cu(*x*)-C12A7 catalysts by PXRD and N_2 physisorption.

Sample	Lattice parameter[a] (Å)	Crystallite size[b] (nm)	S_{BET} (m^2 g^{-1})	Pore volume[c] (cm^3 g^{-1})
C12A7–600	12.037	26	52[d]	0.31[d]
Cu(0.06)-C12A7–600	12.018	26	45	0.38
Cu(0.12)-C12A7–600	12.024	19	54	0.18
Cu(0.24)-C12A7–600	12.017	20	49	0.26
Cu(0.50)-C12A7–600	12.040	22	56	0.22
Cu(1.00)-C12A7–600	12.043	31	51	0.19
C12A7–800	12.020	47	31[d]	0.26[d]
Cu(0.06)-C12A7–800	12.016	45	22	0.23
Cu(0.12)-C12A7–800	12.013	42	22	0.18
Cu(0.24)-C12A7–800	12.014	45	27	0.18
Cu(0.50)-C12A7–800	12.020	47	25	0.22
Cu(1.00)-C12A7–800	12.010	53	25	0.20

[a] The crystallite size was estimated from the peak reflection (*2 1 1*) using the Scherrer equation.

[b] The lattice parameter was determined using the cubic symmetry of C12A7 by eq: $a = d_{hkl} \times \sqrt{h^2 + k^2 + l^2}$, where *a* is the lattice parameter (Å), *d* is the basal distance (Å). The Miller indexes (*h, k, l*) correspond to the reflecting plane used to measure the crystallite size as reported in reference JCPDS No. 09-0413.

[c] N_2 volume taken up at 77 K and relative pressure of 0.99.

[d] Data taken from Ref. [23].

perature the amorphous phase content is reduced, which will be confirmed by Raman spectroscopy (vide infra). In addition, with the increase of the calcination temperature, the C12A7 diffraction peaks became narrower and more intense due to the agglomeration and sintering of the grains. As an outcome, the average crystalline size of C12A7 noticeably increases by almost a factor of two (Table 2). Therefore, the calcination temperature offers a way to control the crystallinity and crystal size of Cu-C12A7 materials.

The calculated lattice parameters for undoped and Cu-doped C12A7 catalysts are summarized in Table 2. Regardless of the copper content and the temperature at which they were treated, the samples present unit cell values (~12.0 Å) closer to the most quoted one for synthetic C12A7:2 O^{2-} ($a = 11.989$ Å) [30]. It has been shown that partial cationic substitution of Ca^{2+} ions (1.0 Å) by smaller Cu^{2+} ions (0.73 Å) leads to a contraction of the lattice ($a = 11.974$ Å) [26]. However, the anionic substitution of O^{2-} extra-framework species occluded within the nanocages by another kind of oxygenated species (i.e., OH^-, O_2^-, and O^-) can also promote a contraction of the unit cell (e.g., a = 11.979 Å) [31]. Thus, the correlation between an effective cation doping and the lattice size modification without considering the influence of the anion substitution should be misadvised. In our case, no apparent relationship could be settled between the increase in doping degree and the variation in lattice value. Meanwhile, the slight lattice expansion observed in our materials could be attributed to the presence of structural defects and lower crystallinity as compared to stoichiometric C12A7:O^{2-} synthesized by solid-state reaction [30].

Cu(*x*)-C12A7 catalysts were further examined by Raman spectroscopy to ensure the mayenite structure and the chemical identity of the occluded extra-framework anions within the C12A7 nanocages. Raman spectra recorded for the Cu(*x*)-C12A7 samples annealed at 600 and 800 °C are shown in Fig. 5a and b, respectively. All spectra recorded in the low-spectral region (200–1000 cm^{-1}) display the characteristic Raman modes of the C12A7 framework, which are mostly assigned to the Al-O framework vibrations [32]. The most dominant band attributed to the symmetric vibration mode of Al–O–Al bridged oxygen between $(AlO_4)^{5-}$ tetrahedra usually appeared at 520 cm^{-1} [32], whereas in our samples, it is shown at 513 and 518 cm^{-1} for the sets calcined at 600 and 800 °C, respectively, showing a shift to higher frequencies with the rise of the calcination temperature. Likewise, the bands in the 700–900 cm^{-1} region, ascribed to the Al-O stretching vibrations in the AlO_4 groups, are also displaced to higher wavenumbers. In the spectral range below 500 cm^{-1} , the low-intense bands are broader and less-resolved for the samples set calcined at 600 °C as compared to 800 °C one, where three bands at 268, 310, and 330 cm^{-1} are observed. The latter bands have been related to the Ca breathing mode and the localized vibrations of framework O^{2-} ions [32]. All these observations are mostly related to the prevalence of structural defects (i.e., superficial hydroxyl groups) at low temperatures, which are diminished with raising the temperature, as will be confirmed by the analysis of the OH vibration region (vide infra). Moreover, peaks at 285, 331, and 616 cm^{-1} not attributable to the C12A7 structure are also distinguished in the set calcined at 600 °C (Fig. 5a). These bands were identified as CuO fingerprints and are in close agreement with those band positions reported in the literature at 296, 346, and 631 cm^{-1} [33]. Conversely, in

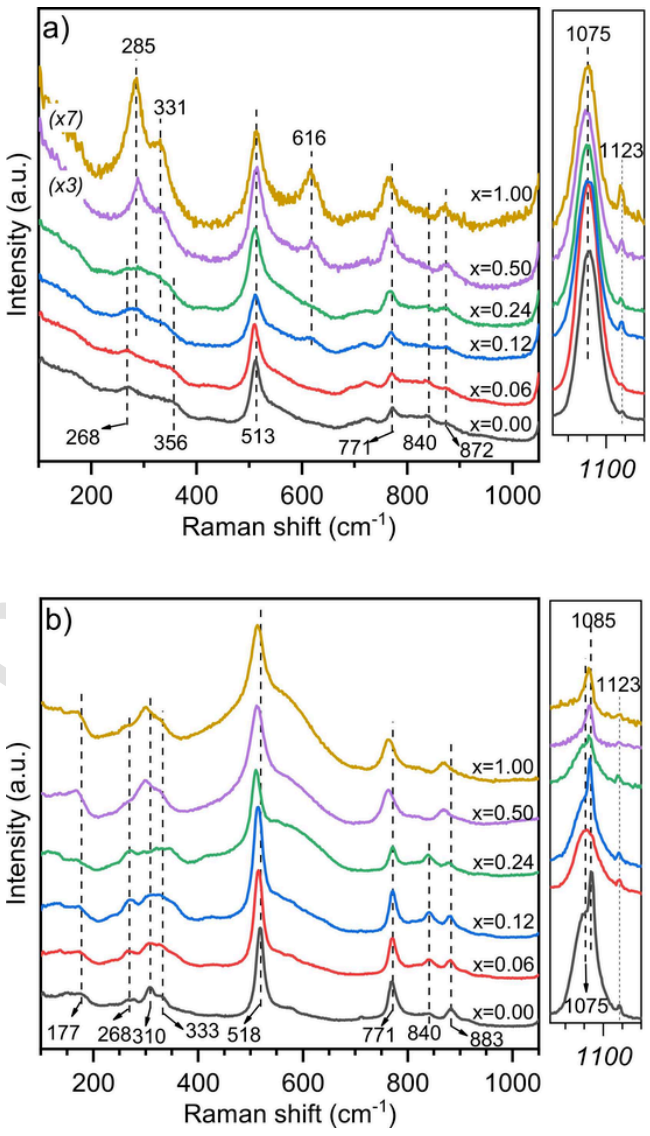

Fig. 5. Raman spectra of Cu-doped C12A7 samples calcined at (a) 600 and (b) 800 °C.

the spectra of the catalysts calcined at 800 °C (Fig. 5b), no CuO-related bands are observed, even for the highest loading ($x = 1.0$), despite the detected presence of CuO crystals by PXRD from $x \geq 0.5$ (Fig. 4). However, a shift to lower frequencies is observed for the C12A7-related bands in the 800 °C set. In addition, the principal mode (Al-O-Al) of the framework vibrations becomes asymmetric with a long low-frequency tail as the doping degree increases. Likewise, the presence of a shoulder at the right side of the principal band is also noted, which evolves and gets broader with rising the Cu loading.

In the region above 1000 cm^{-1} (zoomed regions, Fig. 6a and b), one broad feature centered at 1075 cm^{-1} , sometimes accompanied by a sharp superposed band at 1085 cm^{-1} , is observed in all spectra, regardless of the calcination temperature. Additionally, one small band around 1123 cm^{-1} is also revealed. As previously reported by Che et al., the stretching vibration of superoxide species emerges in the 1075–1195 cm^{-1} range [34]. In the case of C12A7, several studies have assigned a band appearing between 1122 and 1135 cm^{-1} to clathrated O_2^- ions [32,35]. However, other reports have associated the occurrence of O_2^- radicals with a broader band at 1075 cm^{-1} [36,37]. On the contrary, Schmid et al. have shown that lime-based materials display two peaks, one broad and another sharp at 1075 and 1085 cm^{-1}, respectively, which were assigned to the vibration modes of amorphous and crystalline $CaCO_3$ [38]. In this context, it is consistent to ascribe the band at 1123 cm^{-1} to the stretching vibration of O_2^-species in our samples. Concurrently, we have assigned the vibration modes emerging at 1075 and 1085 cm^{-1} to the presence of carbonated CaO rather than O_2^-, which is in line with the existence of CaO in our samples revealed by PXRD (Fig. 4). It can also be noticed that the band at 1075 cm^{-1} is more predominant in the set calcined at 600 °C, whereas in the 800 °C series its intensity decreases with rising the copper loading, which is undoubtedly related to the presence of amorphous domains as shown by PXRD analyses. Differences among the catalysts in each set, in terms of O_2^- concentration, cannot be drawn from the Raman spectra, but their relative concentration will be discussed in the EPR section (vide infra).

In the high-frequency region related to the hydroxyl groups, three peaks around 3570, 3614, and 3680 cm^{-1} are observed in the spectra of both series, as depicted in Fig. A.4 (see Appendix A). The presence of a broad weak band rising from the background below 3550 cm^{-1} can also be observed in the series annealed at 600 °C, especially at the lowest Cu loading ($x = 0.06$). The occurrence of extra-framework OH^- ions in Cu-C12A7 catalysts is confirmed by the band at ~3570 cm^{-1} , which is attributed to the O-H stretching vibrations of OH^- inside the nanocavities of C12A7 [26,39]. The existence of OH^- ions inside the cages of our catalysts can be explained by two factors. (i) The annealing was performed under an ambient atmosphere (i.e., in the presence of atmospheric humidity during the calcination), and (ii) C12A7 is produced by the decomposition of a hydrated precursor (C3AH6), which releases water upon heating. Therefore, it is reasonable that a large amount of OH^- would be inserted in the cages of C12A7, noting the high hydration enthalpy of the material [39]. The two other bands located above 3600 cm^{-1} showing maxima at ~3614 and ~3680 cm^{-1} might be attributed to the presence of structural defects and superficial adsorbed hydroxyls, which can lead to a change in the coordination of a fraction of Al atoms from tetragonal to octahedral [40]. Meanwhile, the weak band below 3550 cm^{-1} has been assigned to the symmetric and antisymmetric vibrations of molecular H_2O adsorbed at the superficial cages of C12A7 [41]. Consequently, the rise of these bands in the hydroxyl region and their connections with structural defects in C12A7 aims to corroborate our observations linked to the band shifts of the Al-O vibrations.

3.2.2. N_2 physisorption analysis

The impact of the calcination temperature and doping degree on the textural properties was studied by N_2 physisorption. The adsorption-desorption isotherms of Cu(x)-C12A7 catalysts heat-treated at 600 and 800 °C containing different copper doping degrees are given in Fig. 6a and b, respectively, whereas the detailed textural properties are listed in Table 2.

All isotherms exhibit a type IV shape and a hysteresis loop of type H3 (Fig. 6). The isotherms shape is typically associated with mesoporous material, while the steep N_2 uptake near P/Po = 1 is connected to the N_2 adsorption within the interparticle spaces between the constituting particles forming aggregates. Besides, the hysteresis loop shape can be attributed to capillary condensation in a non-rigid texture within the interparticle voids, and cannot be assigned to any intra-particular mesoporosity [42]. The latter observations are in agreement with our previous study related to the production of pristine porous C12A7, where aggregates of flake-shaped nanoparticles were found [23]. In the catalysts set calcined at 600 °C, it can be noticed that a large hysteresis loop in the lower relative pressure region (P/Po ~ 0.5–0.8) is present, except for the sample with the lowest copper content ($x = 0.06$), which is associated with the condensation-decondensation of N_2 within smaller mesopores. On the other hand, the catalysts calcined at high temperatures (800 °C) display a narrower hysteresis loop in the same

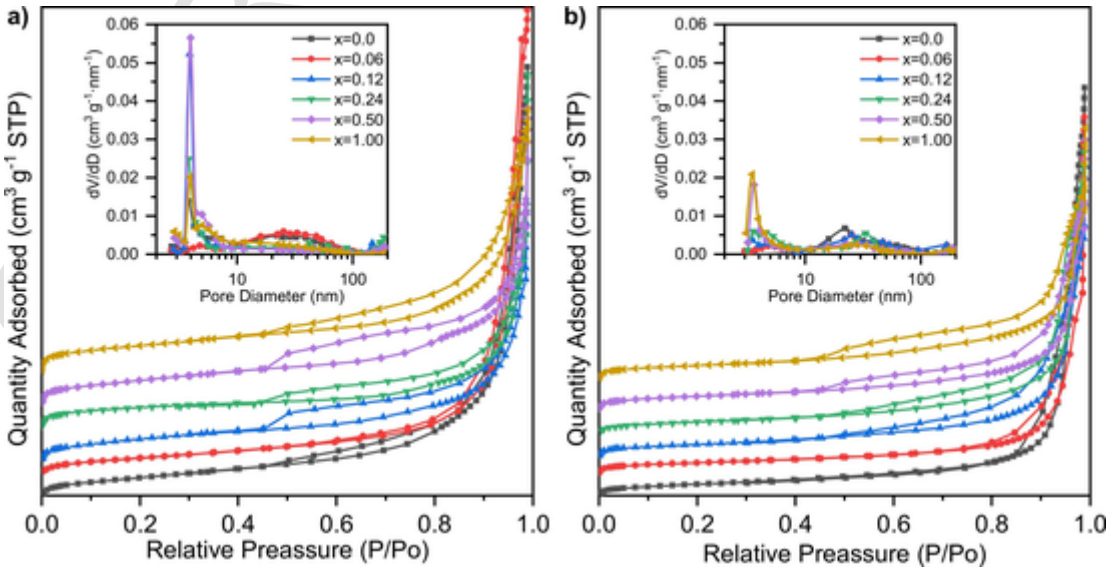

Fig. 6. N_2 physisorption isotherms of Cu(x)-C12A7 catalysts calcined (a) 600 and (b) 800 °C. Pore size distributions (PSD) based on the desorption branch are shown in insets. The isotherms are Y-axis offset to facilitate their visualization.

region. Besides, within the latter set, a shift in the hysteresis loop towards lower P/Po values can be noticed as the doping degree is raised, which is not the case for the former set of the examined catalysts. These findings are in accordance with the analysis of pore size distributions (PSD), where two groups of pores are revealed (insets, Fig. 6). The first group presents a narrow distribution of mesopores showing a maximum at ca. 3.5–4 nm, whereas the second group is characterized by a large PSD in the range between ca. 10–100 nm associated with the interparticle porosity. The former group of pores predominantly appears in the catalysts calcined at 600 °C, whereas at 800 °C, these small mesopores are diminished and tend to fade out as the doping degree is decreased. A similar tendency is also observed in the pore volume (P_v) values among the two sets. The specific surface area (S_{BET}) also reveals a noticeable difference between the two series as a function of the calcination temperature. For instance, the Cu(*x*)-C12A7 catalysts annealed at 600 °C display specific surface area values up to two-fold higher than those treated at 800 °C, which is in line with our previous report related to the production of pristine porous C12A7 [23]. Nevertheless, no correlation between the variation of the doping degree and the S_{BET} values was found in neither of the two sets of catalysts.

The above-described modifications in the textural properties (PSD, S_{BET}, and P_v) among each set with rising the copper loading and between the two sets by increasing the calcination temperature are here discussed. For instance, the series calcined at 600 °C showed the presence of an amorphous phase associated with carbonated amorphous moieties, as corroborated by PXRD and Raman. Yet, the relative content of this amorphous fraction tends to diminish with rising copper loading and the calcination temperature. Similarly, in the series calcined at 800 °C, the increase in the doping degree promoted the crystallization of the CaO phase, probably due to the alteration in the stoichiometry by the partial replacement of Ca by Cu atoms. These structural modifications indirectly provoked by the rise in the copper loading are most likely the origin of the alteration of the PSD and mesoporosity. Besides, the changes in S_{BET} values between the two sets are certainly related to the sintering of grains and agglomeration of the particles due to a rise in the calcination temperature, as shown by PXRD (Fig. 4) where sharper diffractions lines and bigger average particles sizes were found in the set calcined at higher temperature (Table 2).

3.2.3. X-ray photoelectron spectroscopy (XPS) analysis

XPS measurements were conducted to evaluate the Cu surface dispersion and the homogeneity of the different Cu(x)-C12A7 catalysts. Fig. 7 shows the XPS Cu 2p doublet spectra of both sets of samples (600 and 800 °C). The two peaks of the doublets appear at binding energies (BE) of ca. 932–934 eV for a first, and at higher BE between ca. 952–954 eV for the second, corresponding to the Cu $2p_{3/2}$ and Cu $2p_{1/2}$ components, respectively. Besides, a small broad shakeup satellite appears close to the Cu $2p_{3/2}$ peak at higher BE at around 242 eV, which becomes more noticeable as the copper content is increased ($x \geq 0.5$). The occurrence of this satellite peak has been recognized as a distinctive feature of Cu (II) species [43]. Consequently, whatever the copper loading and the calcination temperature, the same typical Cu 2p profile is observed, presenting a $2p_{3/2}/2p_{1/2}$ doublet and a satellite, which corresponds mainly to Cu^{2+} cationic species. Yet, a subtle shift to lower BE in the Cu $2p_{3/2}$ peak is noticed (Fig. 7), as compared to the reported BE value for bulk CuO (933.6 ± 0.4 eV) [43]. The individual BE values for the Cu $2p_{3/2}$ peak summarized in Table 3 corroborate the latter observation, which could be attributed to a partial reduction of the Cu (II) species due to the ultrahigh-vacuum or the photoionization inside the XPS chamber. Since only small BE shifts between the different copper species can be expected, the decomposition of the Cu $2p_{3/2}$ peak to accurately evaluate the Cu speciation (Cu^{2+}, Cu^{+}, and Cu^{0}) is likely to be avoided due to the overlapping binding energies when Cu^{2+} is the most abundant species [43].

Table 3 shows the surface atomic Cu/(Cu + Ca + Al) ratios for all catalysts calculated based on the XPS surface elemental quantifications tabulated in Table A.1 (see Appendix A). The Cu quantification was performed based on the decomposition of Cu 2p spectra considering the Cu $2p_{3/2}$ peak and its satellite. Bulk (nominal) and surface (XPS) atomic Cu/(Cu + Ca + Al) ratios are very close for the Cu(x)-C12A7–600 °C catalysts set, suggesting that a good homogeneity was obtained, excepting for the sample with the highest copper loading ($x = 1.0$) where a lower surface ratio is observed. On the contrary, at

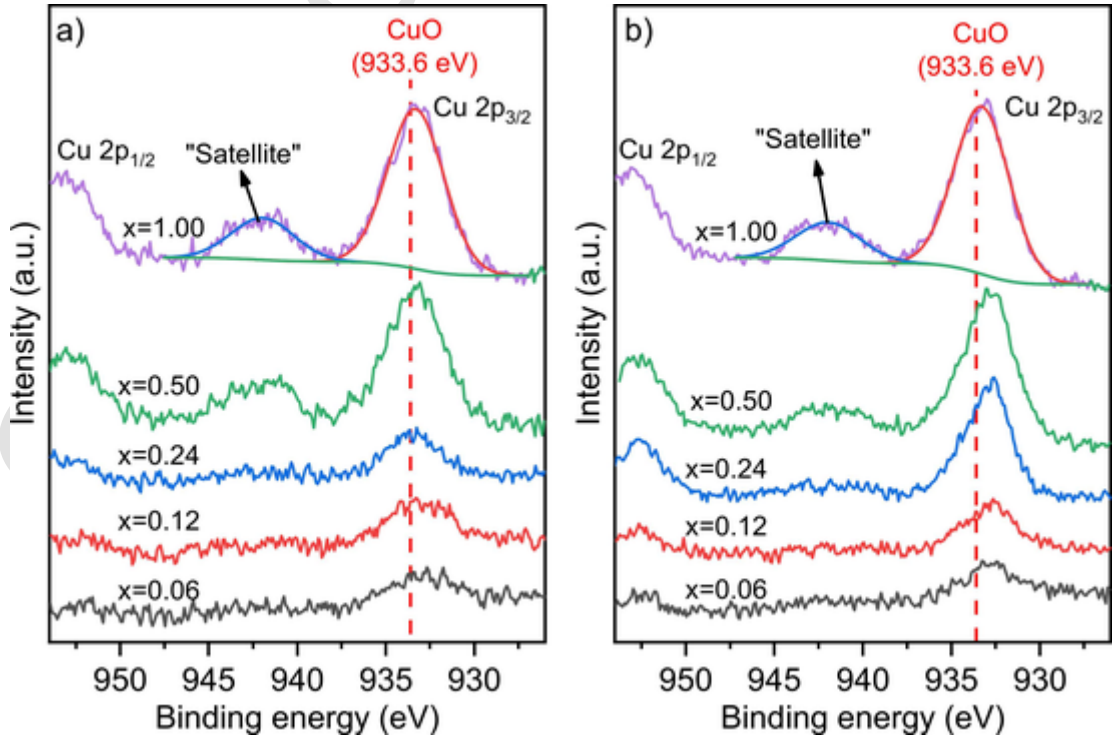

Fig. 7. Cu 2p region XPS spectra of the Cu(*x*)-C12A7 catalysts calcined at (a) 600 and (b) 800 °C.

Table 3
Cu $2p_{3/2}$ binding energy (BE), bulk atomic ratios based on the nominal doping degree (x), and surface atomic ratios based on XPS elemental quantification.

Sample	Cu $2p_{3/2}$ BE (eV)	Bulk Cu/ (Ca + Cu + Al) atomic ratio	Surf. Cu/ (Ca + Cu + Al) atomic ratio	Surf. carbonates/ (Ca + Cu) atomic ratio
Cu(0.06)-C12A7–600	933.0	0.002	0.004	0.51
Cu(0.12)-C12A7–600	933.2	0.005	0.004	0.53
Cu(0.24)-C12A7–600	933.5	0.009	0.008	0.55
Cu(0.50)-C12A7–600	933.3	0.019	0.016	0.42
Cu(1.00)-C12A7–600	933.3	0.038	0.014	0.36
Cu(0.06)-C12A7–800	932.8	0.002	0.004	0.21
Cu(0.12)-C12A7–800	932.9	0.005	0.008	0.23
Cu(0.24)-C12A7–800	932.9	0.009	0.016	0.18
Cu(0.50)-C12A7–800	932.9	0.019	0.028	0.16
Cu(1.00)-C12A7–800	933.3	0.038	0.026	0.26

high temperature (800 °C), the Cu surface content is increased, displaying surface atomic Cu/(Cu + Ca + Al) ratios almost two-fold superior to the bulk ratios. This is probably due to the migration of copper from the inner volume of the catalysts to their surface due to the rise in the temperature during the calcination. In both series, the maximum Cu surface content is reached at the intermediate Cu loading $x = 0.5$, yet from thereon, the rising trend of Cu surface concentration with increasing x is disrupted, showing inferior Cu contents at the highest loading $x = 1$. The latter might be interpreted as a decrease in CuO dispersion as a result of the production of bigger particles (segregated CuO crystallites). The XPS measurements also confirm that the surface content of adventitious carbonate moieties decreases with the rise in the calcination temperature (Table 3), which is consistent with PXRD and Raman observations.

3.2.4. Assignment and quantification of Cu^{2+} and O_2^- species by electron paramagnetic resonance (EPR) spectroscopy

EPR measurements were performed to investigate the nature of the copper species and the influence of the calcination temperature on the relative distribution of the different copper species and superoxide (O_2^-) ions present in the two series of Cu(x)-C12A7 catalysts. Fig. 8 shows the EPR spectra obtained at 77 K for the two series of Cu-doped C12A7 catalysts annealed at 600 (a) and 800 °C (b). All EPR spectra, regardless of the doping degree and calcination temperature, are composed of the same overlapped asymmetric signals ascribable to the paramagnetic Cu^{2+} and O_2^- ions. In the low magnetic field region (260–310 mT), a main axial signal (denoted as A) and another one (hereafter A′) contributing to a lower extent are observed, presenting a four-line hyperfine structure as illustrated by their parallel components (A_{zz}) due to the interactions of odd electrons with copper nuclei ($S = 1/2$, $I = 3/2$) [44,45]. Meanwhile, the perpendicular features of these axial signals (A and A′) appear between 320 and 340 mT, exhibiting broad line widths with unresolved hyperfine splitting structure. Besides, a broad superimposed anisotropic signal (denoted as B) between ca.300–330 mT is also detected. The latter presents large line widths, which have been ascribed to the dipolar interactions between neighboring Cu^{2+} ions accommodated inside Cu(II)-containing aggregates of oxidic type [44,45]. Yet, considering that antiferromagnetic coupling between Cu^{2+} ions within well-crystallized large CuO particles produces EPR silent species, signal B is reasonably ascribed to small clusters where this antiferromagnetic character is not fully established [44,45]. On the other hand, in the high magnetic field region (~330–340 mT), a sharper signal is present in both sets of catalysts. According to previous literature, this feature is assigned to g_{xx} and g_{yy} components of the orthorhombic signal belonging to O_2^- ions clathrated inside the C12A7 cages, whereas the g_{zz} feature is covered under the dominant perpendicular component of the Cu^{2+} species [26]. The intensity of the superoxide signal is superior in the spectra of the catalysts calcined at high temperatures (800 °C), suggest-

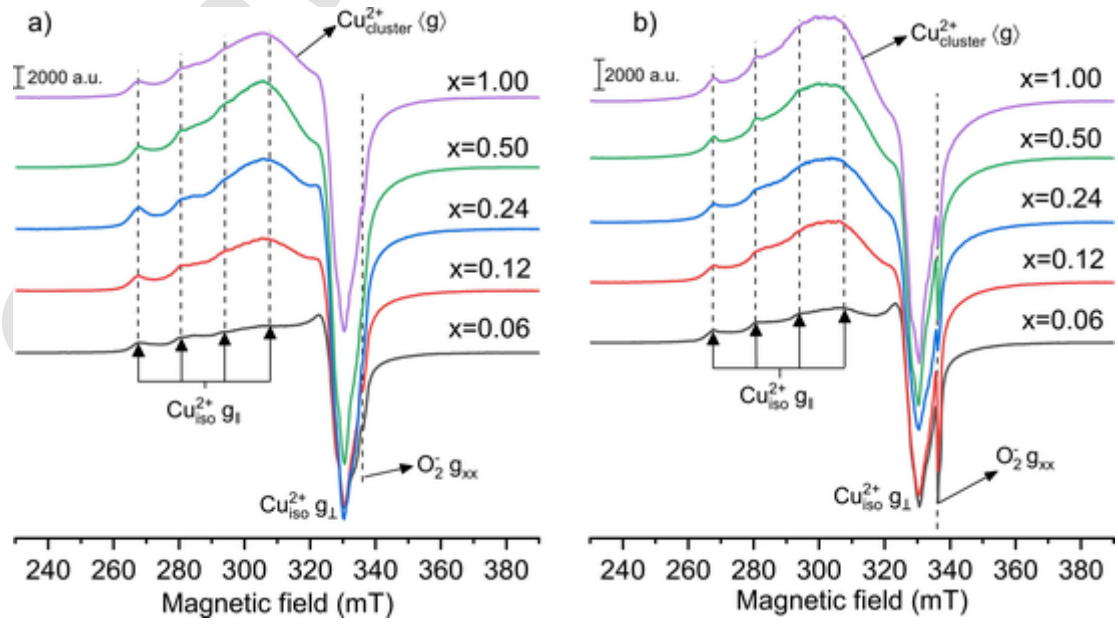

Fig. 8. EPR spectra of two sets of Cu(x)-C12A7 catalysts calcined at (a) 600 and (b) 800 °C.

ing that the rise in the temperature promotes the formation of this oxygenated species presumably due to a partial dehydroxylation of OH^- ions inside cages at the outermost layer of the grains, which was already understood to occur from Raman spectroscopy. Similarly, higher O_2^- concentrations were observed in pristine C12A7 ($x = 0$) annealed at higher temperatures (see Appendix A, Fig. A.5).

Based on computer simulations of the experimental spectra, the fitted EPR parameters are reported in Table 4. The ***g***-tensor values of the A and A′ signals correspond well to those previously reported for isolated Cu^{2+} ions within the C12A7 framework occupying the atomic site of Ca^{2+} ions [26]. Moreover, the observed unresolved hyperfine splitting of the perpendicular component of both signals is attributed to the line bonding associated with the microheterogeneity in the local structural environment of Cu(II) species accommodated in the C12A7 framework [26]. On the other hand, the average ***g***-tensor, $\langle g \rangle = 2.16$, for signal B is similar to those of signals A and A′, confirming that signal B belongs to Cu (II) ions. Finally, the determined ***g***-tensors for O_2^- ions are in good agreement with those found in the literature [32], confirming their assignment.

Fig. 9a shows the absolute concentration of EPR active copper species (Cu^{2+}_{iso} and $Cu^{2+}_{clusters}$) normalized by the catalyst mass determined by the double integration of the spectra and compared with the $CuSO_4$ standard. In both sets, the specific concentration of the EPR active copper species increases monotonically with rising the doping degree. Yet, for the catalysts calcined at 600 °C, a superior concentration and a steeper increase are noticed, attaining a maximum value at $x = 0.5$, then the concentration drops from thereon. Our interpretation is that the excess of Cu induces the formation of bulky CuO species diminishing the dispersion and prompting the agglomeration of the small clusters at the surface of C12A7, which produces a loss in the integral EPR intensity. As aforesaid, these larger CuO particles are EPR-undetectable, thus decreasing the EPR signal concerning the Cu loading. This statement is confirmed by the presence of segregated CuO at higher doping degrees ($x \geq 0.5$) as shown by PXRD.

Fig. 9b displays the relationship between the doping degree and the total amount of EPR active Cu^{2+} species normalized by the nominal number of Cu atoms (Cu_{total}). Consequently, if all the Cu atoms loaded in each catalyst were detected by EPR, this ratio should be equal to 1 (100%). Even though the EPR active Cu^{2+}/Cu_{total} proportion is close to the expected value at the lowest doping degree ($x = 0.06$), as the doping degree increases this ratio declines monotonically, with a loss of nearly ten-fold at the highest x value. This observation confirms that an increase in the doping degree unambiguously promotes the formation of bigger CuO particles due to the coalescence and aggregation of the well-dispersed Cu^{2+} species (isolated and clusters). Meanwhile, the loss of dispersion is intensified at higher temperature due to the migration of Cu atoms from the bulk to the surface, as confirmed by XPS.

Lastly, Fig. 10 assembles the relative contribution of each paramagnetic species (Cu^{2+} isolated, Cu^{2+} cluster, and O_2^-) concerning the normalized total spin concentration shown in Fig. 9a, which was obtained by computer simulation. The clustered Cu^{2+} ions are the most abundant species, except at the lowest Cu loading ($x = 0.06$), where nearly equivalent contributions between the isolated and the clustered Cu^{2+} species are observed, being even slightly predominant at lower temperatures (600 °C). As a result, raising the calcination temperature and the Cu loading promote the production of Cu^{2+} clusters while diminishing the isolated ones. On the other hand, the contribution of superoxide ions (~10^{16}–10^{17} spin g^{-1}, inset Fig. 10) is marginal regarding the absolute spin concentration (~10^{19} spin g^{-1}), yet higher concentrations are detected at elevated temperatures (800 °C), which is associated with a higher partial replacement of OH^- by O_2^- via an anionic-exchange due to the dehydroxylation occurring from ~500 °C [39].

Table 4
EPR parameters of copper (II) and superoxide paramagnetic species in Cu(x)-C12A7 catalysts obtained by computer simulation of the spectra.

Signal	g-tensors				Hyperfine structure constant[b]	
	g_{xx}	g_{yy}	g_{zz}	$\langle g \rangle$[a]	A_{xx}[c] (MHz)	A_{zz} (MHz)
isolated Cu^{2+} (A)	2.071	2.071	2.350		426	15
isolated Cu^{2+} (A′)	2.066	2.066	2.309		512	16
clustered Cu^{2+} (B)				2.16		
O_2^- (superoxide)	2.005	2.008	2.074			

[a]Average ***g***-tensor for the anisotropic signal B.
[b]$A(MHz) = 2.802495 \times g/g_e \times A(G)$, where $g_e = 2.00232$.
[c]$A_{xx} = A_{yy}$ considering an axial symmetry..

3.3. Nature and role of the different Cu (II) species

Considering the distinct nature of the Cu species interacting at different degrees with C12A7, a plausible correlation of their nature with their role in catalytic soot oxidation is here discussed. Two parameters seem to have a significant impact on the catalytic activity of Cu(*x*)-C12A7 materials toward the combustion of soot: (i) the calcination tem-

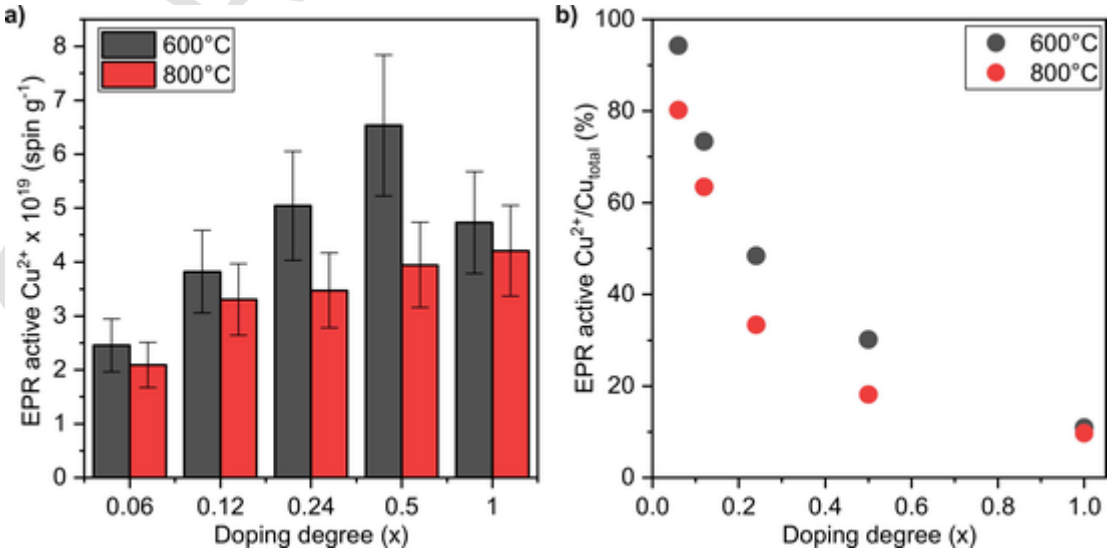

Fig. 9. (a) Total concentration of EPR active Cu^{2+} ions as a function of the doping degree. (b) Relationship between the EPR active Cu^{2+}/Cu_{total} and the doping degree, where Cu^{2+}/Cu_{total} represents the relation between the EPR active Cu^{2+} species to the nominal copper loading.

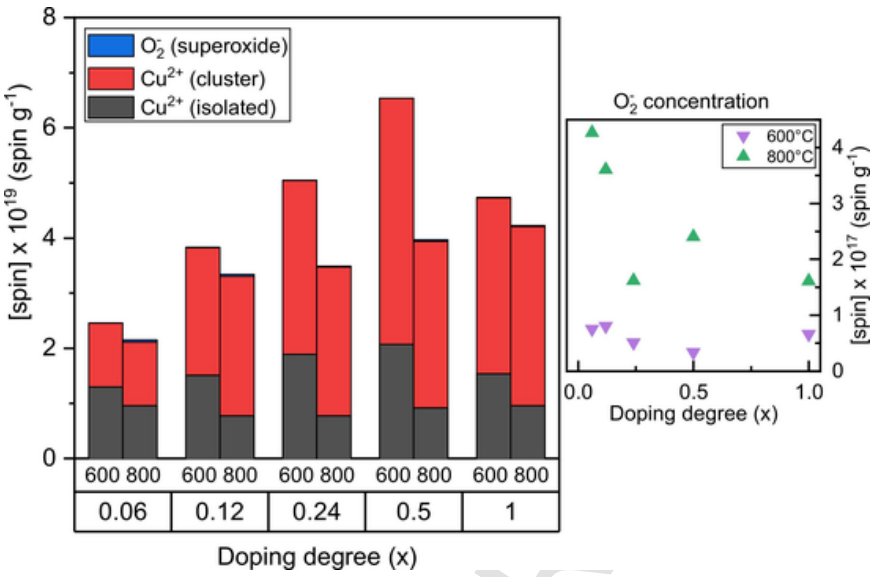

Fig. 10. Contribution of signals Cu^{2+} isolated, Cu^{2+} cluster and O_2^- extracted from computer simulations of the EPR spectra of Fig. 8, as a function of the doping degree for the two series of Cu(x)-C12A7 catalysts. For a better visualization the superoxide concentrations are shown in the inset.

perature; (ii) the nature, abundance, and dispersion of copper. As shown in the previous sections by EPR, Raman, PXRD, and XPS analyses, copper is present as fully oxidized (Cu^{2+}) in three structurally different Cu(II) entities: well-dispersed Cu^{2+} species (isolated and clustered) and segregated CuO particles, whose relative concentrations vary as a function of the doping degree and the calcination temperature.

At low doping degrees ($0 < x < 0.24$), only ca. 60–95% of the total nominal amount of copper was detected and characterized by EPR. For instance, the slightly predominant presence of isolated Cu^{2+} was only observed at low temperatures (600 °C) and low Cu loading ($x = 0.06$). The residual EPR-undetected copper fraction, which was superior in samples calcined at higher temperatures (800 °C), could be due to the presence of small CuO particles, considering that Cu species magnetically interacting with each other, decreases the EPR intensity [44]. Concerning the catalytic performance of the samples in this Cu loading range, an improved catalytic activity, gauged by lower T_{peak} and T_{50} values, was observed as the Cu loading was raised. This positive effect could be related to the increase in the relative concentration of clustered Cu^{2+} species since the content of isolated ones remain almost the same within each set of catalysts with the increasing nominal copper content. On the contrary, the noticed differences in the catalytic activity, at equivalent doping degrees between the two series of catalysts calcined at 600 and 800 °C, could be associated with the superior specific surface area exhibited by the samples calcined at lower temperatures, as previously reported for pristine C12A7 [23].

Moreover, by increasing the Cu content ($x \geq 0.24$), the occurrence of a separated CuO crystalline phase was detected from $x = 0.24$ and $x = 0.5$ for the catalysts calcined at 600 and 800 °C, respectively. Thus, confirming the association of the undetected fraction with the formation of segregated CuO particles, which grow with the excess of Cu via the coalescence and agglomeration of the well-dispersed Cu (II) species, as shown by EPR, Raman, and XRD. Similarly, when rising the Cu loading, the catalytic activity continued to improve until $x = 0.5$, where the lowest T_{peak} values were attained in both series of catalysts. Meanwhile, any Cu excess from thereon hampered the catalytic activity. These evolutions of the catalytic performance might be related to two factors: (i) the highest concentration of EPR Cu^{2+} active species (predominant Cu^{2+} clusters) was also achieved at $x = 0.5$, (ii) the segregated CuO reaches the maximum at the highest loading ($x = 1.0$).

In previous studies related to the catalytic behavior of supported CuO materials in several reaction systems such as soot combustion, NO_x reduction and CO oxidation, the ameliorated catalytic performances of these Cu-promoted catalysts were associated with the formation of CuO amorphous films (Cu^{2+} clusters) over the surface of the support. It was suggested that clustered Cu (II) is easily reduced due to the presence of both Cu-O-Metal and Cu-O-Cu interactions, while the isolated Cu^{2+} species strongly interacting with the support are less reducible due to their instability in a reductive environment and the absence of Cu-O-Cu interactions. On the contrary, the loss of dispersion due to the agglomeration of copper, and thus the formation of segregated bulky CuO particles, notably reduces the Cu-O-Metal interactions, which negatively impacts the redox capacity of the catalysts [44–47]. Therefore, we may speculate that in our case, the three structurally different Cu species located at the surface of C12A7 interact in a similar way as those in the other CuO-supported systems, explaining the catalytic activity enhancement with the increase of clustered Cu^{2+} species, while the activity loss is attributed to the lower interactions between the segregated CuO particles with C12A7. Moreover, the comparable catalytic activity displayed by the Cu(0.50)-C12A7–600 and Cu(0.50)-C12A7–800, although the one calcined at 800 °C presented a lower concentration of clustered Cu species and lower surface area, could be attributed to the higher concentration of superoxide ions promoted by the annealing at elevated temperatures (inset, Fig. 10). In a previous study, Sato et al. suggested that the incorporation of Cu as a dopant in a Si-containing C12A7 enhanced the reactivity of the occluded native O_2^- species [22]. Thus, we may propose that a synergic effect between the well-dispersed Cu^{2+} species and the clathrated O_2^- ions in our catalysts improves the catalytic activity.

3.4. Influence of water on the catalytic performance of Cu(x)-C12A7 catalysts and stability

Considering that water vapor is unavoidably present in combustion exhaust gases, including those of gasoline engines, it is necessary to corroborate that the above-stated observations and findings concerning our catalysts tested in the soot oxidation under dry conditions (5% O_2/He) remain consistent when working under more representative conditions (i.e., in the presence of water vapor). Therefore, several specimens from the series of catalysts calcined at 800 °C were tested under wet conditions (5% H_2O + 5% O_2/He). The selected water content in this study falls in the range of those reported in the literature (i.e., 1–30%) to simulate the composition of the exhaust gases from a diesel combustion engine [48–50]. The conversion soot profile results are displayed in Fig. A.6 (see Appendix A) and the activity indicators are compared

Table 5
Soot activity indicators comparison for Cu(x)-C12A7–800 catalysts tested under dry and wet conditions.

Catalyst	Doping degree (x)	Wet conditions					Dry conditions				
		T_{10} (°C)	T_{50} (°C)	T_{90} (°C)	T_{peak} (°C)	S_{CO_2} (%)	T_{10} (°C)	T_{50} (°C)	T_{90} (°C)	T_{peak} (°C)	S_{CO_2} (%)
Cu(0.00)-C12A7–800	0.00	436	476	511	474	99	448	503	547	514	91
Cu(0.06)-C12A7–800	0.06	430	476	511	480	99	443	491	531	496	92
Cu(0.50)-C12A7–800	0.50	408	439	469	437	100	416	460	498	464	100
Cu(1.00)-C12A7–800	1.00	416	450	489	445	100	425	474	515	486	100

(wet vs dry conditions) in Table 5. Above all, the previously observed relationship between the doping degree and the catalytic activity under dry conditions remains unchanged in the presence of water, showing that the best catalytic activity is achieved at a copper loading equal to 0.5 where the clustered Cu^{2+} species are dominant. The presence of water in the reaction medium accelerates the reaction rate for all the tested catalysts, regardless of the copper content. As shown in Fig. A.6 (see Appendix A), all soot conversion profiles obtained under wet conditions are shifted to low temperatures as compared to those acquired under dry conditions. The latter is confirmed by the activity indicators summarized in Table 5. For instance, lower T_{50} values were achieved when soot was oxidized in the presence of water vapor. Moreover, water also seems to promote the formation of CO_2 over CO, as observed at low copper loadings where lower CO_2 selectivity values were obtained under dry conditions. These improvements in the catalytic oxidation of soot related to the introduction of water in the reaction medium have been already reported in previous studies [48–50]. For instance, it has been reported that the presence of water during the oxidation of soot is much more important that is concentration in the exhaust gases [48]. In a recent isotopic study [50], Yang et al. proposed that water participates in the soot oxidation reaction as an accelerator rather than as an oxidant. They suggested that the improved soot activity under wet conditions is associated with (i) the easier capability of water to be adsorbed and dissociated at the surface of the catalyst in comparison to dioxygen, and (ii) its ability to boost the regeneration of oxygen vacancies. Besides, C12A7 is known for its capacity of hosting inside its cages a wide variety of anions. Among them, OH^- ions are easily formed by an anionic exchange reaction between water and oxygen radicals inside C12A7, when the material is annealed in an atmosphere containing water in a wide range of temperatures (~400–900 °C) [39]. Therefore, we suggest that the superficial cages might act as active sites in the formation of OH*, which promotes the formation of surface-oxygen complexes (SOCs) at the contact points between the surfaces of C12A7 and primary soot particles, boosting the catalytic activity. However, this hypothesis needs to be corroborated, which is the subject of an ongoing investigation.

The long-term stability of our best catalyst, Cu(0.50)-C12A7–800 (x = 0.5), has been tested in four consecutive soot combustion cycles under dry (O_2/He) and wet (H_2O/O_2/He) conditions, and the obtained T_{50} values in each run are reported in Fig. A.7 (see Appendix A). The catalytic activity under dry conditions showed to remain almost unchanged after 4 cycles, demonstrating the robustness of our catalyst. Besides under wet conditions, a slight deactivation (if significant) was observed during the first three cycles, yet from thereon the catalytic behavior remained stable.

4. Conclusions

We successfully prepared Cu-doped C12A7 materials presenting well-dispersed Cu^{2+} species and improved textural properties via a one-pot solution combustion synthesis. Cu loading and calcination temperature noticeably affected the relative abundance of the different Cu species, their degree of dispersion, and the textural and structural properties of the Cu-C12A7 catalysts, which significantly influence their catalytic performance in the soot oxidation. Cu-doped C12A7 catalysts contained three structurally distinct forms of copper species: isolated Cu^{2+}, clusters of Cu^{2+}, and segregated CuO particles. Cu-doped C12A7 catalysts were notably more active than the bare C12A7 one, with an optimal doping level of x = 0.5, also showing an improved selectivity towards CO_2 with rising the Cu loading. We suggested that the enhancement in the catalytic activity is due to the increase in the relative concentration of the well-dispersed clustered Cu^{2+} species interacting with C12A7. An excessive doping degree diminished the catalyst performance due to the loss of dispersion and segregation of CuO. Overall, identically under dry as wet conditions, an appropriate balance of the dispersion degree of the Cu species, textural properties, and superoxide species of the Cu-doped C12A7 catalysts allows an improvement of their catalytic performance in the soot oxidation reaction. The presence of water vapor during the soot oxidation reaction showed a positive effect on the catalytic performance of our catalysts, but the relationship performance-Cu species remained identical under wet and dry conditions. Although the Cu-doped C12A7 catalysts are slightly less efficient compared to conventional catalysts such as CeO_2 or supported noble metals, the latter catalysts are composed of rare, critical, and expensive elements, whereas the former ones are based on abundant and inexpensive elements (Ca and Al) and only contain small copper contents (2.3%wt for x = 0.5). Thus, this likely compensates for their slightly lower activity, as their lower value allows for increasing the amount of loaded catalyst in the filter trap. Another possibility to boost the activity of our Cu-doped C12A7 materials could be the preparation of three-dimensional ordered macroporous (3-DOM) structured catalysts to promote the contact between soot and catalyst particles. Additionally, the reflected long-term thermal stability of Cu-doped C12A7 makes it a promising candidate to uphold the high temperatures attained inside the catalytic filter at localized hot spots.

CRediT authorship contribution statement

Isaac Meza-Trujillo: Writing – original draft, Conceptualization, Methodology, Investigation, Formal analysis, Visualization. **Arnaud Mary:** Investigation, Formal analysis. **Piotr Pietrzyk:** Validation, Resources, Writing – review & editing. **Zbigniew Sojka:** Writing – review & editing. **Eric M. Gaigneaux:** Conceptualization, Supervision, Resources, Project administration, Funding acquisition, Writing – review & editing.

Declaration of Competing Interest

The authors declare that they have no known competing financial interests or personal relationships that could have appeared to influence the work reported in this paper.

Acknowledgments

We thank the UCLouvain (Université catholique de Louvain, Belgium) for the CAI (Conseil d'Action International) grant in the frame of the doctoral program “Coopération au développement” and for the extension grant “Mandats de fin de thèse 2020” due the COVID-19 pandemic, both awarded to I. Meza-Trujillo. The "Académie de recherche et d’enseignement supérieur" (ARES, Belgium) is also acknowledged for

the scholarship awarded to I. M.-T. in the frame of the "Programme de mobilité 2019-2020" via the "Commission coopération au développement (CCD)" . We also thank the "Federation Wallonie-Bruxelles" (Belgium) for the travel grant (Bourse de voyage - Appel 2018 / BV18-15) awarded to I.M.-T. to perform the EPR and Raman analyses at the Jagiellonian University (Krakow, Poland). We acknowledge Dr. F. Devred for his valuable technical and scientific support. We are thankful for the precious help given by A. Krasowska and Dr. K. Sobańska during the EPR and Raman measurements.

References

[1] European Automobile Manufacturers Association, Fuel Types of New Cars: Petrol 47.5%, Hybrids 12.4%, Electric 9.9% Market Share Third Quarter 2020, 2020. ⟨https://www.acea.be/press-releases/article/fuel-types-of-new-cars-petrol-47.5-hybrids-12.4-electric-9.9-market-share-t⟩, (Accessed 26 March 2021).

[2] United States Environmental Protection Agency, Particulate Matter (PM) Pollution, Part. Matter Pollut. (n.d.). ⟨https://www.epa.gov/pm-pollution⟩, (Accessed 26 March 2021).

[3] Publications Office of the European Union, EURO-lex, Regul. No 715/2007 Eur. Parliam. Counc. 20 June 2007 Type Approv. Mot. Veh. with Respect to Emiss. from Light Passeng. Commer. Veh. (Euro 5 Euro 6) Access to Veh. Repair Mai., 2007, pp. 1–16. ⟨https://eur-lex.europa.eu/legal-content/EN/TXT/?uri=CELEX%3A02007R0715-20200901⟩, (Accessed 26 March 2021).

[4] B. Giechaskiel, A. Joshi, L. Ntziachristos, P. Dilara, European regulatory framework and particulate matter emissions of gasoline light-duty vehicles: a review, Catalysts 9 (2019), https://doi.org/10.3390/catal9070586.

[5] D. Fino, S. Bensaid, M. Piumetti, N. Russo, A review on the catalytic combustion of soot in Diesel particulate filters for automotive applications: from powder catalysts to structured reactors, Appl. Catal. A Gen. 509 (2016) 75–96, https://doi.org/10.1016/j.apcata.2015.10.016.

[6] A. Bueno-López, Diesel soot combustion ceria catalysts, Appl. Catal. B Environ. 146 (2014) 1–11, https://doi.org/10.1016/j.apcatb.2013.02.033.

[7] D. Fino, N. Russo, G. Saracco, V. Specchia, The role of suprafacial oxygen in some perovskites for the catalytic combustion of soot, J. Catal. 217 (2003) 367–375, https://doi.org/10.1016/S0021-9517(03)00143-X.

[8] J. Oi Uchisawa, A. Obuchi, Z. Zhao, S. Kushiyama, Carbon oxidation with platinum supported catalysts, Appl. Catal. B Environ. 18 (1998) L183–L187, https://doi.org/10.1016/S0926-3373(98)00046-0.

[9] J. Oi-Uchisawa, A. Obuchi, S. Wang, T. Nanba, A. Ohi, Catalytic performance of Pt/MOx loaded over SiC-DPF for soot oxidation, Appl. Catal. B Environ. 43 (2003) 117–129, https://doi.org/10.1016/S0926-3373(02)00296-5.

[10] V. Alcalde-Santiago, A. Davó-Quiñonero, D. Lozano-Castelló, A. Bueno-López, On the soot combustion mechanism using 3DOM ceria catalysts, Appl. Catal. B Environ. 234 (2018) 187–197, https://doi.org/10.1016/j.apcatb.2018.04.023.

[11] V. Alcalde-Santiago, E. Bailón-García, A. Davó-Quiñonero, D. Lozano-Castelló, A. Bueno-López, Three-dimensionally ordered macroporous PrOx: an improved alternative to ceria catalysts for soot combustion, Appl. Catal. B Environ. 248 (2019) 567–572, https://doi.org/10.1016/j.apcatb.2018.10.049.

[12] Q. Wu, J. Xiong, Y. Zhang, X. Mei, Y. Wei, Z. Zhao, J. Liu, J. Li, Interaction-induced self-assembly of Au@La_2O_3 core-shell nanoparticles on $La_2O_2CO_3$ nanorods with enhanced catalytic activity and stability for soot oxidation, ACS Catal. 9 (2019) 3700–3715, https://doi.org/10.1021/acscatal.9b00107.

[13] J. Xiong, X. Mei, J. Liu, Y. Wei, Z. Zhao, Z. Xie, J. Li, Efficiently multifunctional catalysts of 3D ordered meso-macroporous $Ce_{0.3}Zr_{0.7}O_2$-supported PdAu@CeO_2 core-shell nanoparticles for soot oxidation: synergetic effect of Pd-Au-CeO_2 ternary components, Appl. Catal. B Environ. 251 (2019) 247–260, https://doi.org/10.1016/j.apcatb.2019.03.078.

[14] T. Andana, M. Piumetti, S. Bensaid, L. Veyre, C. Thieuleux, N. Russo, D. Fino, E.A. Quadrelli, R. Pirone, Ceria-supported small Pt and Pt_3Sn nanoparticles for NO_x-assisted soot oxidation, Appl. Catal. B Environ. 209 (2017) 295–310, https://doi.org/10.1016/j.apcatb.2017.03.010.

[15] S. Liu, X. Wu, W. Liu, W. Chen, R. Ran, M. Li, D. Weng, Soot oxidation over CeO_2 and Ag/CeO_2: factors determining the catalyst activity and stability during reaction, J. Catal. 337 (2016) 188–198, https://doi.org/10.1016/j.jcat.2016.01.019.

[16] Z. Yang, N. Zhang, Y. Cao, M. Gong, M. Zhao, Y. Chen, Effect of yttria in Pt/TiO_2 on sulfur resistance diesel oxidation catalysts: enhancement of low-temperature activity and stability, Catal. Sci. Technol. 4 (2014) 3032–3043, https://doi.org/10.1039/C4CY00424H.

[17] T. Andana, M. Piumetti, S. Bensaid, L. Veyre, C. Thieuleux, N. Russo, D. Fino, E.A. Quadrelli, R. Pirone, CuO nanoparticles supported by ceria for NO_x-assisted soot oxidation: insight into catalytic activity and sintering, Appl. Catal. B Environ. 216 (2017) 41–58, https://doi.org/10.1016/j.apcatb.2017.05.061.

[18] J. Liu, Z. Zhao, C. ming Xu, A. jun Duan, Simultaneous removal of NO_x and diesel soot over nanometer Ln-Na-Cu-O perovskite-like complex oxide catalysts, Appl. Catal. B Environ. 78 (2008) 61–72, https://doi.org/10.1016/j.apcatb.2007.09.001.

[19] I. Atribak, F.E. López-Suárez, A. Bueno-López, A. García-García, New insights into the performance of ceria-zirconia mixed oxides as soot combustion catalysts. Identification of the role of "active oxygen" production, Catal. Today 176 (2011) 404–408, https://doi.org/10.1016/j.cattod.2010.11.023.

[20] J. Gryboś, M. Fedyna, P. Legutko, B. Leszczyński, J. Janas, A. Wach, J. Szlachetko, X. Yu, A. Kotarba, Z. Zhao, Z. Sojka, Mechanistic insights into oxygen dynamics in soot combustion over cryptomelane catalysts in tight and loose contact modes via $^{18}O_2/^{16}O_2$ isotopic variable composition measurements-a hot ring model of the catalyst operation, ACS Catal. 11 (2021) 9530–9546, https://doi.org/10.1021/acscatal.1c02152.

[21] V. Alcalde-Santiago, A. Davó-Quiñonero, E. Bailón-García, D. Lozano-Castelló, A. Bueno-López, Copper-lanthanum catalysts for NOx and soot removal, ChemCatChem 12 (2020) 6375–6384, https://doi.org/10.1002/cctc.202001187.

[22] K. Sato, M. Yamaguchi, S. Fujita, K. Suzuki, T. Mori, Enhancement of the activity of calcium aluminosilicate ($Ca_{12}Al_{10}Si_4O_{35}$) for the combustion of diesel soot via the substitution of Ca^{2+} ions with transition metal ions, Catal. Commun. 7 (2006) 132–135, https://doi.org/10.1016/j.catcom.2005.09.005.

[23] I. Meza-Trujillo, F. Devred, E.M. Gaigneaux, Production of high surface area mayenite (C12A7) via an assisted solution combustion synthesis (SCS) toward catalytic soot oxidation, Mater. Res. Bull. 119 (2019) 110542, https://doi.org/10.1016/j.materresbull.2019.110542.

[24] S. Yang, J.N. Kondo, K. Hayashi, M. Hirano, K. Domen, H. Hosono, Partial oxidation of methane to syngas over promoted C12A7, Appl. Catal. A Gen. 277 (2004) 239–246, https://doi.org/10.1016/j.apcata.2004.09.030.

[25] J.R. Salasin, C. Rawn, Structure property relationships and cationic doping in $[Ca_{24}Al_{28}O_{64}]^{4+}$ framework: A review, Crystals 7 (2017) 1–25, https://doi.org/10.3390/cryst7050143.

[26] S. Maurelli, M. Ruszak, S. Witkowski, P. Pietrzyk, M. Chiesa, Z. Sojka, Spectroscopic CW-EPR and HYSCORE investigations of Cu^{2+} and O_2^- species in copper doped nanoporous calcium aluminate ($12CaO{\cdot}7Al_2O_3$), Phys. Chem. Chem. Phys. 12 (2010) 10933–10941, https://doi.org/10.1039/c0cp00084a.

[27] J. Huang, L. Valenzano, G. Sant, Framework and channel modifications in mayenite ($12CaO{\cdot}7Al_2O_3$) nanocages by cationic doping, Chem. Mater. 27 (2015) 4731–4741, https://doi.org/10.1021/acs.chemmater.5b01360.

[28] T. Spalek, P. Pietrzyk, Z. Sojka, Program EPRsim32, J. Chem. Inf. Model. 45 (2005) 18–29.

[29] A. Bueno-López, K. Krishna, M. Makkee, J.A. Moulijn, Active oxygen from CeO_2 and its role in catalysed soot oxidation, Catal. Lett. 99 (2005) 203–205, https://doi.org/10.1007/s10562-005-2120-x.

[30] H. Bartl, T. Scheller, Zur Struktur des $12CaO{\cdot}7Al_2O_3$, Neues Jahrb. Miner. (1970) 547–552.

[31] H. Boysen, M. Lerch, A. Stys, A. Senyshyn, Structure and oxygen mobility in mayenite ($Ca_{12}Al_{14}O_{33}$): a high-temperature neutron powder diffraction study, Acta Crystallogr. Sect. B Struct. Sci. 63 (2007) 675–682, https://doi.org/10.1107/S0108768107030005.

[32] K. Kajihara, S. Matsuishi, K. Hayashi, M. Hirano, Hideo Hosono, Vibrational dynamics and oxygen diffusion in a nanoporous oxide ion conductor $12CaO{\cdot}7Al_2O_3$ studied by ^{18}O labeling and micro-Raman spectroscopy, J. Phys. Chem. C 111 (2007) 14855–14861, https://doi.org/10.1021/jp074248n.

[33] L. Debbichi, M.C. Marco De Lucas, J.F. Pierson, P. Krüger, Vibrational properties of CuO and Cu_4O_3 from first-principles calculations, and raman and infrared spectroscopy, J. Phys. Chem. C 116 (2012) 10232–10237, https://doi.org/10.1021/jp303096m.

[34] M. Che, A.J. Tench, Characterization and reactivity of molecular oxygen species on oxide surfaces, Adv. Catal. 32 (1983) 1–148, https://doi.org/10.1016/S0360-0564(08)60439-3.

[35] S. Yang, J.N. Kondo, K. Hayashi, M. Hirano, K. Domen, H. Hosono, Formation and desorption of oxygen species in nanoporous crystal $12CaO{\cdot}7Al_2O_3$, Chem. Mater. 16 (2004) 104–110, https://doi.org/10.1016/j.ssi.2004.07.057.

[36] S. Fujita, M. Ohkawa, K. Suzuki, H. Nakano, T. Mori, H. Masuda, Controlling the quantity of radical oxygen occluded in a new aluminum silicate with nanopores, Chem. Mater. 15 (2003) 4879–4881, https://doi.org/10.1021/cm030562s.

[37] A. Intiso, J. Martinez-Triguero, R. Cucciniello, F. Rossi, A.E. Palomares, Influence of the synthesis method on the catalytic activity of mayenite for the oxidation of gas-phase trichloroethylene, Sci. Rep. 9 (2019) 1–9, https://doi.org/10.1038/s41598-018-36708-2.

[38] T. Schmid, P. Dariz, Shedding light onto the spectra of lime: Raman and luminescence bands of CaO, $Ca(OH)_2$ and $CaCO_3$, J. Raman Spectrosc. 46 (2014) 141–146, https://doi.org/10.1002/jrs.4622.

[39] K. Hayashi, M. Hirano, H. Hosono, Thermodynamics and kinetics of hydroxide ion formation in $12CaO{\cdot}7Al_2O_3$, J. Phys. Chem. B 109 (2005) 11900–11906, https://doi.org/10.1021/jp050807j.

[40] E.V. Galuskin, J. Kusz, T. Armbruster, R. Bailau, I.O. Galuskina, B. Ternes, M. Murashko, A reinvestigation of mayenite from the type locality, the Ettringer Bellerberg volcano near Mayen, Eifel district, Germany, Mineral. Mag. 76 (2012) 707–716, https://doi.org/10.1180/minmag.2012.076.3.18.

[41] D. Środek, M. Dulski, I. Galuskina, Raman imaging as a new approach to identification of the mayenite group minerals, Sci. Rep. 8 (2018) 1–14, https://doi.org/10.1038/s41598-018-31809-4.

[42] M. Thommes, K. Kaneko, A.V. Neimark, J.P. Olivier, F. Rodriguez-Reinoso, J. Rouquerol, K.S.W. Sing, Physisorption of gases, with special reference to the evaluation of surface area and pore size distribution (IUPAC technical report), Pure Appl. Chem. 87 (2015) 1051–1069, https://doi.org/10.1515/pac-2014-1117.

[43] M.C. Biesinger, Advanced analysis of copper X-ray photoelectron spectra, Surf. Interface Anal. 49 (2017) 1325–1334, https://doi.org/10.1002/sia.6239.

[44] P.G. Harrison, I.K. Ball, W. Azelee, W. Daniell, D. Goldfarb, Nature and surface redox properties of copper(II)-promoted cerium(IV) oxide CO-oxidation catalysts, Chem. Mater. 12 (2000) 3715–3725, https://doi.org/10.1021/cm001113k.

[45] A. Martínez-Arias, M. Fernández-García, J. Soria, J.C. Conesa, Spectroscopic study of a Cu/CeO_2 catalyst subjected to redox treatments in carbon monoxide and oxygen, J. Catal. 182 (1999) 367–377, https://doi.org/10.1006/jcat.1998.2361.

[46] M. Sakai, Y. Nagai, Y. Aoki, N. Takahashi, Investigation into the catalytic reduction of NO at copper–ceria interface active sites, Appl. Catal. A Gen. 510 (2016) 57–63, https://doi.org/10.1016/j.apcata.2015.11.007.
[47] X. Feng, R. Liu, X. Xu, Y. Tong, S. Zhang, J. He, J. Xu, X. Fang, X. Wang, Stable $CuO/La_2Sn_2O_7$ catalysts for soot combustion: study on the monolayer dispersion behavior of CuO over a $La_2Sn_2O_7$ pyrochlore support, Chin. J. Catal. 42 (2021) 396–408, https://doi.org/10.1016/S1872-2067(20)63657-9.
[48] C. Sun Park, M.W. Lee, J.H. Lee, E.J. Jeong, S.H. Lee, J.W. Choung, C.H. Kim, H.C. Ham, K.Y. Lee, Promoting effect of H_2O over macroporous Ce-Zr catalysts in soot oxidation, Mol. Catal. 474 (2019) 110416, https://doi.org/10.1016/j.mcat.2019.110416.
[49] J.M. Christensen, J.D. Grunwaldt, A.D. Jensen, Effect of NO_2 and water on the catalytic oxidation of soot, Appl. Catal. B Environ. 205 (2017) 182–188, https://doi.org/10.1016/j.apcatb.2016.12.024.
[50] W. Yang, Y. Wang, H. Wang, Y. Zhang, Y. Peng, J. Li, Water accelerates and directly participates soot oxidation: an isotopic study, Appl. Catal. B Environ. 302 (2022) 120837, https://doi.org/10.1016/j.apcatb.2021.120837.